Ann. Geophys., 35, 161–170, 2017
www.ann-geophys.net/35/161/2017/
doi:10.5194/angeo-35-161-2017

Annales Geophysicae Open Access EGU

Climatology of thermospheric neutral winds over Oukaïmeden Observatory in Morocco

Mohamed Kaab[1], Zouhair Benkhaldoun[1], Daniel J. Fisher[2], Brian Harding[2], Aziza Bounhir[1], Jonathan J. Makela[2], Amine Laghriyeb[1], Khalifa Malki[1], Ahmed Daassou[1], and Mohamed Lazrek[1]

[1]Oukaimeden Observatory, Laboratoire de Physique des Hautes Energies et Astrophysique, FSSM, Cadi Ayyad University, Marrakech, Morocco
[2]Department of Electrical and Computer Engineering, University of Illinois at Urbana-Champaign, Urbana, Illinois, USA

Correspondence to: Mohamed Kaab (mohamed.kaab@edu.uca.ma)

Received: 30 August 2016 – Revised: 5 January 2017 – Accepted: 5 January 2017 – Published: 30 January 2017

Abstract. In order to explore coupling between the thermosphere and ionosphere and to address the lack of data relating to thermospheric neutral winds and temperatures over the African sector, a new system of instruments was installed at the Oukaïmeden Observatory located in the high Atlas Mountains, 75 km south of Marrakesh, Morocco (31.206° N, 7.866° W, 22.84° N magnetic). In this work we present the first multi-year results of the climatology of meridional and zonal winds obtained during the period from January 2014 to February 2016, including observations from 648 nights. The measurements are obtained using an imaging Fabry–Pérot interferometer, which measures the 630.0 nm emissions caused by dissociative recombination of O_2^+. The basic climatology of the winds is as expected, showing zonal winds that are strongly eastward in the early evening just after sunset with a speed of 50 to 100 m s^{-1} decreasing in magnitude, and reversing directions in the local summer months, towards sunrise. The meridional winds are slightly poleward in the early evening during the local winter, before reversing directions around 21:00 LT. In the local summer months, the meridional winds are equatorward for the entire night, reaching a maximum equatorward speed of 75 m s^{-1}. We compare the observed climatologies of neutral winds to that provided by the recently updated Horizontal Wind Model (HWM14) in order to validate that model's predictions of the thermospheric wind patterns over the eastern portion of Africa. The model captures much of the features in the observational climatologies. The most notable exception is for the zonal winds during local summer, when the maximum eastward wind in the observations occurs approximately 4 h later than seen in the model results.

Keywords. Ionosphere (ionosphere–atmosphere interactions; ionospheric irregularities) – meteorology and atmospheric dynamics (climatology)

1 Introduction

Space weather is a relatively new field of study and encompasses understanding how the near-space environment responds to forcing from lower-atmosphere weather systems as well as conditions on the Sun. Although the specific effects of space weather – including power grid failures, communication outages, and navigation errors when using space-based navigation systems such as the Global Positioning System – are local in nature, understanding and predicting their occurrence requires a global view of the environment. Recognizing this, the United Nations has sponsored the International Space Weather Initiative (ISWI), a multi-national program focused on advancing the understanding of space weather through the global deployment of space weather sensors and the development of competencies within the developing world to work in this relatively new field.

ISWI was created as a follow-up activity after the successful International Heliophysics Year (IHY) in 2007 (Thompson et al., 2009). The ISWI is a program of international collaboration which aims to develop the scientific and experimental tools for understanding and predicting the weather of the near-Earth space environment. To address the need for global coverage of measurements, the ISWI has brought together a variety of instrument providers and hosts from around the world to build an unprecedented observing net-

work for space weather science. In comparison to other regions of the globe, the African sector has historically received the least amount of attention in terms of ground-based ionospheric/thermospheric measurements. Most studies that present statistics of space weather effects in the African sector are based upon satellite data (e.g., Huang et al., 2001; Burke et al., 2004). As pointed out in Makela et al. (2004) and Makela and Miller (2011), however, ground-based statistics and satellite-based statistics can vary significantly. This is because a satellite in situ probe only makes measurements at the location of a spacecraft as it moves through a specific region at a specific altitude. In contrast, ground-based measurements provide, essentially, a continual monitoring capability of a given region of the upper atmosphere.

Previous studies have revealed that the African sector presents unique features, not seen in other regions of the world. For example, Hei et al. (2005) analyzed in situ measurements of topside plasma depletions made by the AE-E satellite and found that the African sector is dominated by superchannels, unlike the single- and multichannel-dominated Pacific sector. Furthermore, Yizengaw et al. (2011) noted that the ionospheric $\boldsymbol{E} \times \boldsymbol{B}$ drift velocities were faster in the American sector than the African sector. These studies do not mention how the neutral parameters couple with the plasma to create these features, suggesting that more detailed studies of the thermosphere/ionosphere over Africa are required. Within the past several years, significant ground-based infrastructure has been deployed as part of the ISWI and other initiatives to address the deficiency of measurements in the African sector (e.g., Yizengaw et al., 2013). Despite this progress, critical measurements of thermospheric winds and temperatures are almost completely lacking in this region.

It was within the framework of the ISWI that in November 2013, a team of scientists from the University of Illinois at Urbana-Champaign in the United States deployed a suite of optical instruments at the Oukaïmeden Observatory in the Atlas Mountains near Marrakesh, Morocco (31.206° N, 7.866° W, 22.84° N magnetic). They installed an imaging Fabry–Pérot interferometer (FPI) similar to what is described in Makela et al. (2009) in order to measure the nighttime thermospheric winds and temperatures. These neutral parameters are crucial as they are a key driver of plasma motion. Similar systems previously deployed in other parts of the world have demonstrated their utility in capturing the solar cycle, seasonal, and daily fluctuations of the neutral winds (e.g., Emmert et al., 2006; Meriwether et al., 2011; Brum et al., 2012; Fisher et al., 2015). Combined with data from existing sites in the American sector and elsewhere, the data from Africa will play a critical role in understanding large-scale tidal features in the upper atmosphere as well as understanding longitudinal variability in these larger-scale features. In this paper, we present a 26-month climatology of the neutral winds as well as a comparison to the recently updated Horizontal Wind Model (HWM14; Drob et al., 2015) and to prior measurements made in different longitude sectors but at similar geographic and geomagnetic latitudes.

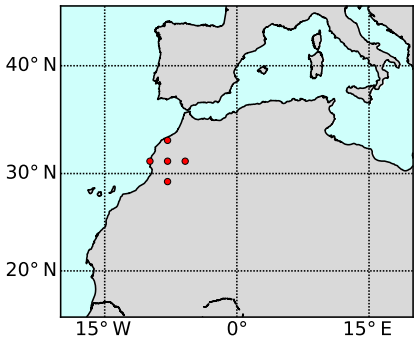

Figure 1. A map of the measurement locations for the Fabry–Pérot interferometer (FPI) in Oukaïmeden Observatory. Each dot represents a possible 250 km observation point of a single FPI measurement.

2 Instrumentation

The FPI is an instrument designed to make highly accurate spectral measurements. The instrument produces a two-dimensional ring pattern on a high-quality CCD, which can be analyzed to produce an estimate of the line shape of an emission. For the case studied here, the emission of interest, selected by a narrowband interference filter in the instrument, is that produced by the dissociative recombination of O_2^+, which naturally occurs in the lower thermosphere peaking at an altitude of about 250 km (Link and Cogger, 1988). The lifetime of the associated emission process is long enough that the emitter thermalizes and, thus, the properties of the emitted photons are indicative of the local thermosphere. Therefore, the spectral shape measured by the FPI can be related to the velocity of the emitting region through a measured Doppler shift, while the temperature can be related to the broadening of the line shape.

The FPI deployed at the observatory has a relatively small field of view ($< 2°$) and so a SkyScanner system is used to steer the field of view to different locations in the sky. The SkyScanner is a pointing system mounted inside a large protective dome. Two mirrors are controlled by a dual-axis motor system to point the field of view in the desired direction. The SkyScanner is controlled by custom software, which also commands the instrument to collect data. A typical observation mode cycles through a series of six specified azimuth and elevation directions (zenith, laser, east, north, west, and south). The integration time for each exposure of the sky is determined based on the previous sky exposure in such a way as to keep the uncertainty less than 10 m s^{-1}. Typical integration time can range from 30 s to 10 min, depending on the brightness of the emission. The "laser" direction denotes an observation made of a frequency-stabilized HeNe

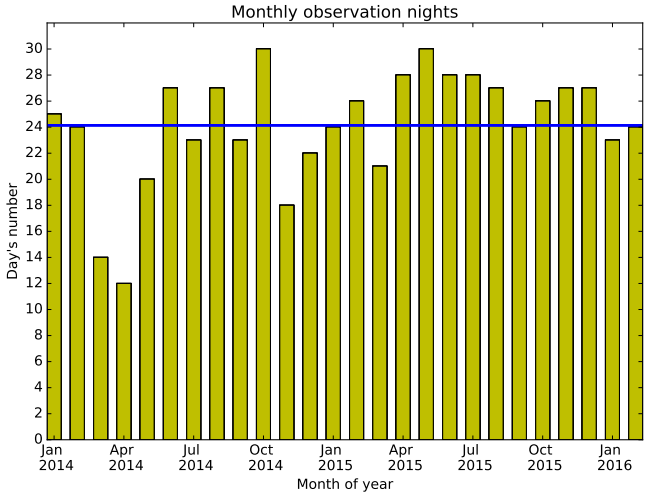

Figure 2. The number of observation nights per month from January 2014 until February 2016. The blue bar denotes the average number of observations obtained each month over the period of study.

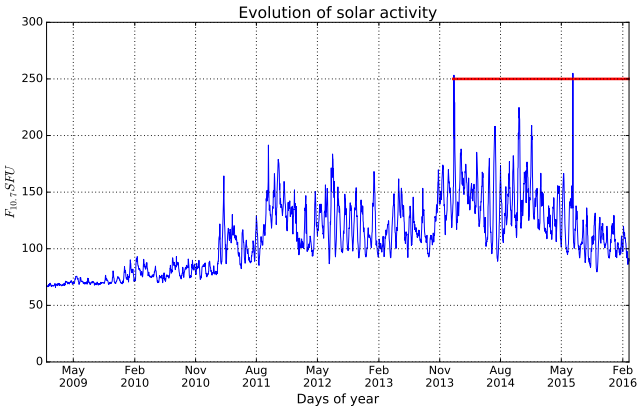

Figure 3. Evolution of the $F_{10.7}$ from January 2009 to February 2016 with the period of available data (red).

laser, which is used to monitor the stability of the instrument and provide an estimate of the instrument's optical transfer function (see Makela et al., 2011). The laser observations, contained with the observations made towards zenith over the entire night, are used to establish the unknown zero-Doppler reference. Given the estimated instrument function and zero-Doppler reference, observations in the four cardinal directions can be analyzed to produce estimates of the horizontal thermospheric neutral winds, using the method described in Harding et al. (2014). Estimates of the zonal (meridional) winds are made from the observations to the east and west (north and south) and are assumed to be representative of that wind component at the location where the given line-of-sight intersects the emitting layer, assumed to occur at 250 km altitude. This observing geometry is shown in Fig. 1.

3 Data and analysis

After deployment of the instrumentation and an initial testing period at the end of 2013, useful observations of the instrument began in January 2014. Figure 2 shows the number of usable observing nights for the 26 months used in this study. A total of 648 nights were collected, giving a monthly average equal to 24 nights a month (the blue bar in Fig. 2), representing a significant database from which climatological averages will be derived in this study. These nights extend the initial climatologies presented by Fisher et al. (2015), where the first year of observations from this site was presented. The period covered in the present study coincides with a period of decreasing solar activity covering the end of the maximum of solar cycle 24 through its declining phase, as shown in Fig. 3 (the red bar denotes the time during which observations presented here were made). Given the excellent observing conditions at the observatory, full coverage of all four seasons was obtained.

In order to create climatologies, we adopted the method detailed in Fisher et al. (2015). Following this, we eliminate all non-physical values in the measured neutral winds that are not automatically removed from initial processing. For the zonal winds we removed values greater than 200 m s^{-1} and less than -100 m s^{-1}, and for the meridional winds we removed values greater than 150 m s^{-1} and less than -150 m s^{-1}. We also remove values if the estimated wind uncertainties are more than 25 m s^{-1}. Finally, we do not consider the observations taken during cloudy periods, as determined by a collocated cloud sensor.

Then, for each month of observation, we sort and bin the filtered data into 30 min intervals and, for each interval, calculate a weighted average, v_m, and sample variability, e, such that

$$v_m = \frac{\sum_i^N v_i . w_i}{\sum_i^N w_i} \quad (1)$$

and

$$e = \left(\frac{1}{N-1} \sum_i^N (v_i - v_m)^2 \right)^{1/2}, \quad (2)$$

where v_i, $w_i = 1/\sigma_i^2$, and N are respectively the value of the wind (zonal or meridional), its weight (the inverse of its uncertainty, σ_i, squared), and the number of measurements in the given bin. All data for a given month, regardless of year, were grouped together in this process.

Examining the meridional winds presented in Fig. 4, we see a clear seasonality, typical of a midlatitude station, in the climatologies. In the local winter months (November–February), poleward speeds of approximately 50 m s^{-1} are

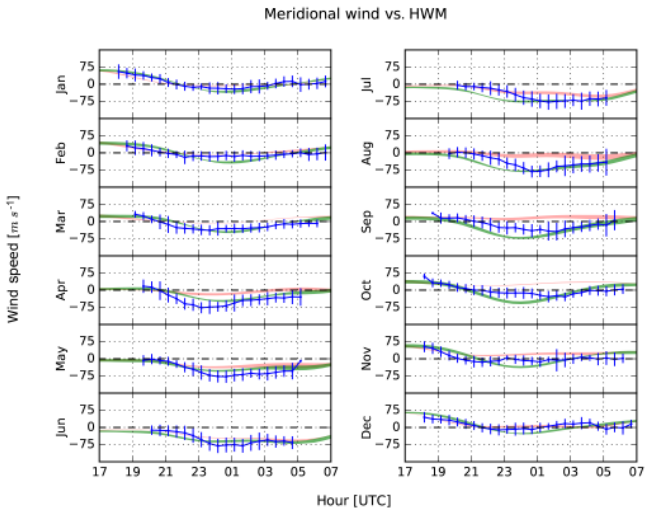

Figure 4. Monthly averages of meridional winds from January 2014 until February 2016 (blue). Airglow-weighted model results from HWM07 (red) and HWM14 (green). Positive values are northward.

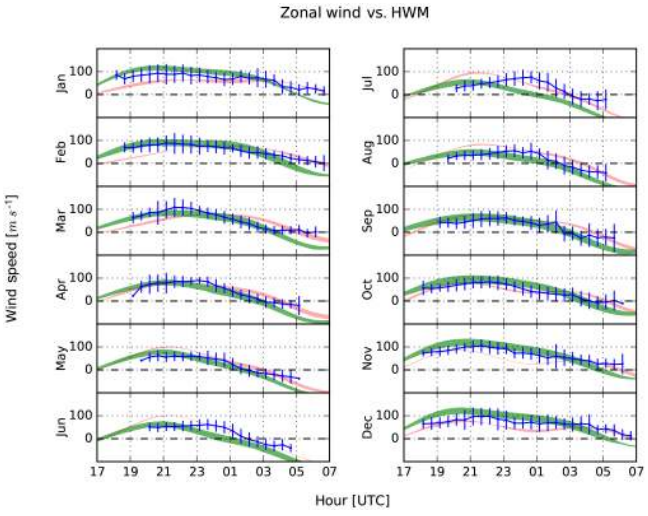

Figure 5. Monthly averages of zonal winds from January 2014 until February 2016 (blue). Airglow-weighted model results from HWM07 (red) and HWM14 (green). Positive values are eastward.

seen in the early evening, reversing to equatorward flow around 21:00 LT. No poleward flow is observed in the local summer months (June–August) post-sunset. Throughout the year, equatorward winds are observed in the middle of the night, having the largest magnitudes in the local summer months (75 m s^{-1}), with negligible meridional flow seen in the middle of the night during the local winter months. The peak in equatorward flow shifts from about 23:00 LT during the spring equinox, to 01:00 LT during the summer solstice, to 02:00 LT during the autumnal equinox. This flow reverses once again, to poleward, between 01:00 and 03:00 LT during the local winter months, but does not fully recover for local summer months, with an equatorward flow of 50 m s^{-1} seen at sunrise from April through August.

Measurements of the zonal winds are presented in Fig. 5. The wind is eastward at the beginning of the night in all seasons and increases for the first several hours after sunset. A maximum eastward speed of 100 m s^{-1} is observed at around 21:00 LT in the local winter months. The maximum eastward flow transitions to later times and smaller amplitudes during the equinox periods and into the local summer, when the maximum eastward flow of 75 m s^{-1} is observed around local midnight. After the maximum eastward flow is reached, a gradual abatement is seen in all months. The wind reverses to westward around 02:00 LT from April through September, reaching a maximum westward flow of around 25 m s^{-1}. A reversal is not seen during the other months.

4 Discussion

4.1 Comparison to climatological models

One source of uncertainty in conducting a comparison of the observed climatologies and the estimated winds provided by an empirical model is that the altitude of the emitting layer, and thus the location of the observations, is unknown for the imaging FPI measurements. Recently, Chartier et al. (2015) performed a study that simulated the thermospheric observations of an FPI using several different models. For simulations of the low-latitude thermosphere, they concluded that incorrectly assigning the altitude of the emission layer could lead to erroneous comparisons and that the largest errors were introduced when the emitting layer was lower than 250 km, due to the larger altitudinal gradients in the winds at low altitudes.

To investigate this potential effect on the observations presented here, we have simulated the altitudinal profiles of the 630.0 nm emission over the Oukaïmeden Observatory during the period studied. Standard climatological models (IRI Bilitza et al. (2014) and MSIS Picone et al. (2002)) are used to provide estimates of the atmospheric constituents required to calculate the redline volume emission rate specified in Link and Cogger (1988). The peak altitude of the emitting layer is then found as a function of hour and day of year. Results are shown in Fig. 6. It is clear that the standard assumption that the emitting layer peaks at an altitude of 250 km is not appropriate most of the time, although one could argue that "on average" it is an appropriate value. Specifically, the layer begins the night relatively low in altitude. By midnight, the peak emission altitude has typically increased by 20–40 km before decreasing to post-sunset altitudes before dawn. Sea-

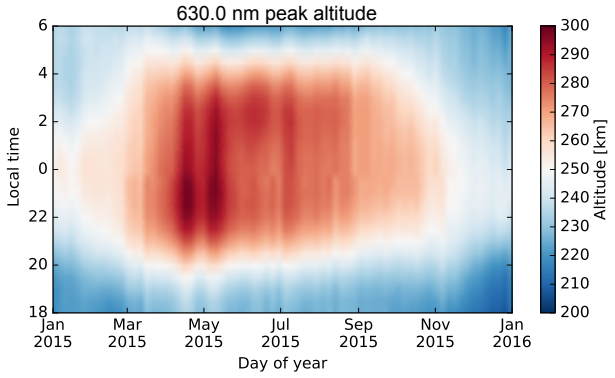

Figure 6. Modeled 630.0 nm emission peak altitude over Oukaïmeden Observatory as a function of local time and day of year during 2015. The emission profile was modeled using the volume emission rate described in Link and Cogger (1988), which requires utilizing the IRI and MSIS models.

sonally, the layer is highest during the local spring and lowest during local winter. Failing to take these dynamics into account could bias the comparison results to a model.

In this section, we compare the monthly climatologies to the thermospheric wind patterns predicted by the Horizontal Wind Model (HWM). This model was recently updated by Drob et al. (2015), with one of the main new data sources in the update being recent FPI data from the American sector. For this sector, the improvement in specifying the thermospheric winds was significant compared to the previous iteration of HWM (HWM07; Drob et al., 2008). Prior comparisons to the imaging FPI observations in the American sector to the HWM07 model had shown significant disagreements (Makela et al., 2012). Since no new ground-based measurements of the thermospheric wind from the African sector were included in the reformulation of HWM14, the comparisons presented here serve as an independent validation for that model.

To account for variability due to the peak airglow layer (mentioned above) in generating monthly statistics, we calculate the airglow-weighted HWM winds for comparison to the observed FPI wind climatologies. Chartier et al. (2015) found that this approach produced more satisfactory results than assuming a fixed altitude of 250 km. Of course, the models used to predict the airglow layer's volume emission rate are empirical models, and so the actual day-to-day variability in the layer altitude will not be captured. However, we are limited by not having actual observations of the layer altitude, or a proxy such as *hm*F2. The airglow-weighted winds are estimated by

$$\hat{u} = \frac{\sum_z u_z a_z}{\sum_z a_z}, \tag{3}$$

where u_z are the horizontal winds from HWM at altitude z and a_z is the calculated redline volume emission rate from Link and Cogger (1988) at altitude z. Both HWM and the models needed for the volume emission rate do vary with local time and season. All presented HWM data have been airglow-weighted in order to provide more robust comparisons with our data.

The meridional wind comparison between the FPI-measured monthly climatologies (blue), airglow-weighted HWM07 winds (red), and airglow-weighted HWM14 winds (green) is presented in Fig. 4. In general, HWM14 correctly captures the trends of the meridional wind pattern described above for the monthly climatologies derived from the observations. That is, the early evening winds in the local winter months are poleward, reducing in magnitude and eventually reversing to equatorward near local midnight, then reducing in magnitude again and reversing to poleward before local sunrise. In the local summer, the initial meridional winds are close to zero, or slightly equatorward, in agreement with the data. Their equatorward magnitude increases towards local midnight, remaining equatorward through the early morning hours. This general agreement is improved as compared to HWM07, especially for August–October, for which HWM07 shows significant disagreement with the observed climatologies. The improvement of HWM14 over HWM07 has been noted in other studies (Liu et al., 2016).

A closer look reveals several disagreements between the observations and HWM14. In April and May, the magnitude of the maximum equatorward flow of HWM14 is underestimated by approximately 30 m s^{-1}. Conversely, in September through November, HWM14 overestimates the magnitude of the maximum equatorward flow by approximately 40 m s^{-1}. We also see disagreement in the early evening hours of July through September, during which the increase in the equatorial wind magnitude occurs earlier in the evening in HWM14 than it does in the observations.

Turning to the zonal winds in Fig. 5, we see general agreement of the measured climatologies and predictions of the empirical model from September through February. The general trend of strong eastward winds in the early evening followed by a general abatement is seen in both the observations and HWM14. However, during these months, the model disagrees with the observations immediately before sunrise, predicting westward winds that are about 50 m s^{-1} stronger than those observed.

The agreement between the observations and HWM14 predictions of the zonal wind is less satisfactory for the other months, especially from June through August. During these months, there appears to be a significant phase shift between the observed maximum in the eastward wind magnitude and that predicted by HWM14. This phase shift is approximately 4 h, with the peak seen at around 20:00 LT in the model and close to midnight in the observations. Similar to the comparisons surrounding the winter solstice discussed above, the predicted zonal winds are significantly more westward immediately before sunrise during the months surrounding the summer solstice.

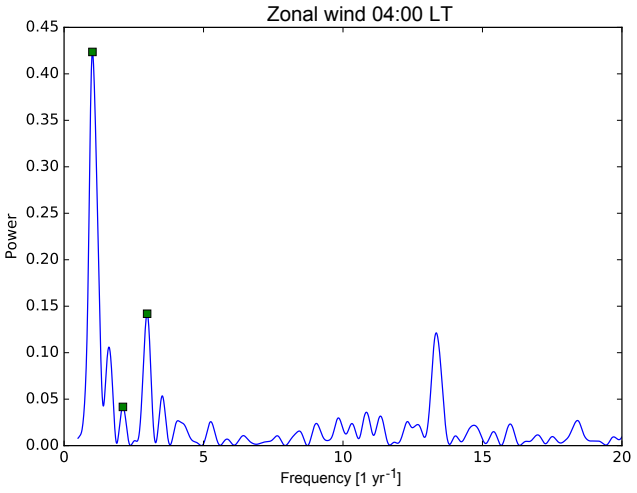

Figure 7. A Lomb–Scargle periodogram of zonal winds over Oukaïmeden Observatory at 04:00 LT. The squares represent the locations of the annual, semiannual, and terannual harmonics.

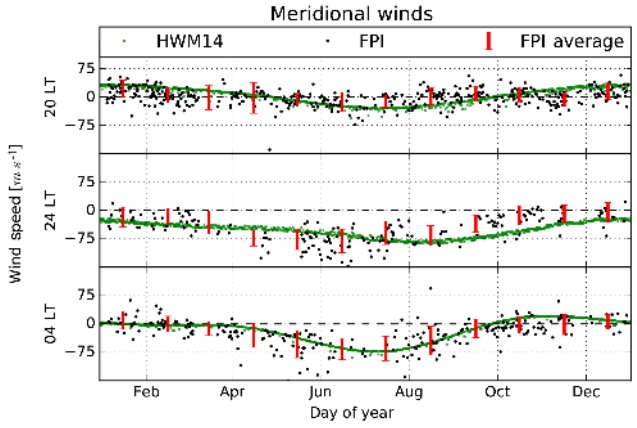

Figure 8. A comparison of measured meridional winds to HWM at fixed local times of 20:00, 24:00, and 04:00. The black dots represent a binned measurement, the red bars represent monthly averaged FPI estimate, and the green dots represent the HWM14 airglow-weighed estimate. Positive values are northward.

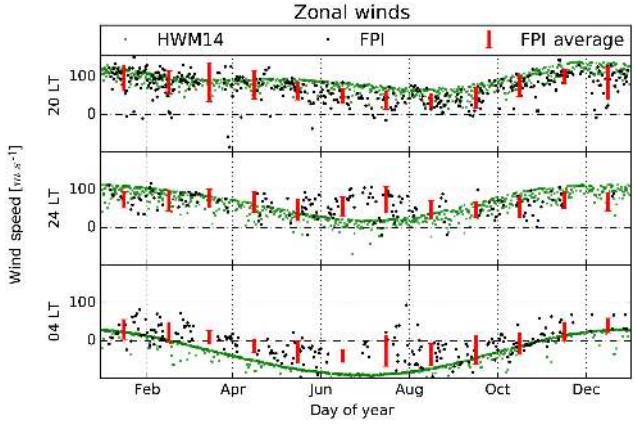

Figure 9. A comparison of measured zonal winds to HWM at fixed local times of 20:00, 24:00, and 04:00. The black dots represent a binned measurement, the red bars represent monthly averaged FPI estimate, and the green dots represent the HWM14 airglow-weighed estimate. Positive values are eastward.

To further investigate the long-term variations in the thermospheric winds and their comparisons to the airglow-weighted HWM14 neutral winds, we perform an analysis to extract the annual, semiannual, and terannual variations in the observations. This analysis is similar to that performed by Yuan et al. (2013) for observations made at Xinglong station, in central China. Comparisons to those observations are described below in Sect. 4.2. Here, we choose to look at three local times over the observation period: pre-midnight (20:00 LT ± 15 min), midnight (24:00 LT ± 15 min), and post-midnight (04:00 LT ± 15 min). We first utilize a fast Lomb–Scargle periodogram to pull out the dominant frequencies from each local time, binning for meridional and zonal winds independently. Figure 7 shows an example of the periodogram produced to find the strength of the harmonics in the wind data. Using this power spectrum, the least-squares model returns a best-fit wave with a period of 1 year. From this wave, we extract an offset and peak amplitude in m s^{-1} as well as phase where the day of year (DOY) reports the location of maximum amplitude. This single harmonic is then subtracted from the observational data to get residuals for another Lomb–Scargle analysis. This cycle repeats for a harmonic fitting for both a 6-month period and then a 4-month period.

We present the daily and seasonal variations in the measured neutral winds against the airglow-weighted HWM14 winds at 20:00, 24:00, and 04:00 LT for meridional and zonal components in Figs. 8 and 9, respectively. Using the results of this analysis, we list the amplitudes and phases from the annual, semiannual, and terannual components of the harmonic reconstruction for both the measured winds and airglow-weighted HWM14 winds in Table 1. The dominant variation seen in the observations is the annual variation, with the exception of the observed zonal winds at 24:00 LT, for which all three components have nearly equal amplitudes. The phase of the observed annual variation is nearly constant for the meridional wind (ranging from day of year 344–355), with a bit more variation seen for the zonal component (ranging from day of year 8–47). The analysis of the HWM14 results also shows a dominant annual variation. However, disagreements in the amplitude of about 20 m s^{-1} and phase of up to almost 50 days between the observations and modeling results are seen. For the amplitude, there is no consistent biasing between the observations and model (that is, the amplitude of the modeled annual variation can be either larger or smaller than the observations). However, the phase for the meridional (zonal) wind is always later (earlier) for the model.

Table 1. The annual, semiannual, and terannual harmonic fits to the meridional and zonal winds for the Moroccan FPI data, HWM07, and HWM14 at 20:00, 24:00, and 04:00 LT. The amplitude is in $m\,s^{-1}$ and the phase (in parentheses) is in DOY.

LT	Period (year)	Meridional wind			Zonal wind		
		FPI	HWM07	HWM14	FPI	HWM07	HWM14
20	1	11.8 (344)	12.9 (301)	29.9 (8)	29.9 (23)	20.2 (199)	25.7 (359)
	1/2	2.4 (45)	5.9 (81)	3.3 (114)	7.6 (130)	19.0 (147)	15.9 (146)
	1/3	7.4 (6)	2.0 (76)	1.0 (121)	5.4 (70)	0.8 (4)	1.5 (90)
24	1	37.8 (346)	27.9 (324)	24.4 (24)	7.9 (47)	14.6 (100)	46.6 (359)
	1/2	5.1 (52)	14.7 (93)	8.9 (148)	8.3 (28)	14.1 (56)	6.4 (105)
	1/3	9.4 (64)	1.3 (98)	0.5 (117)	8.1 (76)	1.1 (16)	0.5 (20)
04	1	39.1 (355)	28.0 (344)	36.0 (356)	36.2 (8)	53.2 (362)	59.6 (359)
	1/2	9.2 (84)	27.0 (91)	18.7 (104)	4.7 (8)	6.6 (54)	3.2 (156)
	1/3	3.6 (4)	1.1 (40)	1.1 (14)	4.9 (66)	0.9 (32)	0.5 (6)

Turning to the terannual variations, we note that as intended, HWM does not fit this 4-month variation. However, the observations indicate that the terannual variation is more significant than the semiannual variation for the early evening meridional wind and of equal importance for the zonal winds. Looking at the phases, we see that there are also significant disagreements between the observations and models for these components. This could be a limitation of the analysis technique used, as the amplitudes of these components are on the order of the uncertainties in the measurements, however, Liu et al. (2016) found that, regionally and seasonally, HWM14 underestimates the neutral winds when compared to GOCE satellite measurements.

4.2 Comparison to prior observations

Since there are such a limited number of Fabry–Pérot observatories, the database containing FPI measurements is somewhat sparse, making it difficult to find direct corollaries. However, there are three prior studies that present data from sites with roughly comparable latitudes as Morocco (31.206° N, 7.866° W, 22.84° N magnetic) and so should share characteristics with the observations presented here. Fisher et al. (2015) presented FPI data from Pisgah Astronomical Research Institute (PARI; 35.2° N, 2.85° W, 47.63° N magnetic). This site is at nearly the same geographic latitude but a very different geomagnetic latitude and longitude sector. Second, there is the work of Brum et al. (2012), which presents a 30-year climatology of thermospheric winds for observations made above Arecibo Observatory in Puerto Rico (18.35° N, 66.75° W, 31.10° N magnetic). This site has a much closer geomagnetic latitude to Oukaïmeden Observatory but is not close geographically in latitude or longitude. Third, is prior work from Yuan et al. (2013) which compared the FPI data from Xinglong station in central China (40.2° N, 117.4° E, 35.57° N magnetic) to HWM07. Though this site is not as close to Oukaïmeden in either geographic or geomagnetic coordinates as either PARI or Arecibo, it is applicable to use as a comparison of how the harmonic analysis at two sites changes between HWM07 and HWM14.

Figure 11 of Fisher et al. (2015) compared the first year of FPI data over the Oukaïmeden Observatory to coincident measurements taken from PARI. The extension of analysis of data from Morocco presented here confirms the initial climatologies presented in this earlier paper. To summarize the comparison presented by Fisher et al. (2015), good agreement was found between the two sites; both sets of observations showed eastward winds all year in the early evening that decay towards a westward reversal before sunrise. They also showed general agreement in the meridional winds being equatorward in local summer and poleward followed by an equatorward reversal during the local winter. However, the magnitude of the winds were shown to be slightly different for the two sites, with the local midnight equatorward winds being stronger over PARI than Morocco. For the zonal winds, differences were seen in the amplitude of the maximum eastward flow (with the winds typically being faster over Morocco) as well as the timing of the reversal from eastward to westward flow (with the reversal taking place 2 h earlier in local time over PARI). Fisher et al. (2015) concluded that, in line with the prior hypothesis presented by Wu et al. (2014), some of these differences were likely attributable to differences in the geomagnetic latitudes of the two sites. This prompts the need to compare the data from Oukaïmeden with data from a site at a similar geomagnetic latitude.

The Arecibo Observatory was chosen because it is closer in geomagnetic latitude to the Oukaïmeden Observatory. Brum et al. (2012) presented an analysis of 30 years of neutral wind measurements made from this site. For comparison, we use results of the seasonal variations in the meridional and zonal winds presented in their Fig. 8. First looking at the meridional data, we see general agreement in all four seasons. The first point of agreement is the flow throughout the local winter and equinox nights; winds start northward and

Table 2. The annual, semiannual, and terannual harmonic fits to the meridional and zonal winds for the Xinglong FPI data (after Table 1 of Yuan et al., 2013), HWM07, and HWM14 at local midnight (24:00 LT). The amplitude is in $m\,s^{-1}$ and the phase (in parentheses) is in DOY.

LT	Period (year)	Meridional wind			Zonal wind		
		FPI	HWM07	HWM14	FPI	HWM07	HWM14
24:00	1	7.0 (238)	15.6 (235)	18.9 (290)	23.0 (2)	17.6 (256)	56.2 (272)
	1/2	3.3 (151)	12.5 (175)	7.5 (87)	5.9 (18)	21.5 (165)	4.2 (138)
	1/3	2.9 (21)	0.8 (119)	0.5 (57)	0.4 (102)	0.8 (16)	0.5 (100)

turn southward, reaching a maximum around local midnight, and finally reversing again before sunrise. While the general pattern is shared between the two sites, the poleward-to-equatorward and equatorward-to-poleward reversals (except when they do not occur in the June solstice) occur earlier and later, respectively over Oukaïmeden. The magnitudes are in agreement for the equinoxes, but during the winter period, the meridional winds over Morocco flow poleward for most of the night, with only slight reversals to equatorward, which is in contrast to Arecibo having a $40\,m\,s^{-1}$ equatorward wind around local midnight.

Next looking at the zonal measurements from Arecibo, we again see general agreement in all four seasons. The winds start eastward, increasing to a maximum value before local midnight, and then slowly decay to $0\,m\,s^{-1}$ (and even reversing in June). The magnitude of peak eastward flow over Arecibo is nearly always $80\,m\,s^{-1}$, while the data collected from Oukaïmeden vary more with season, maximizing at $110\,m\,s^{-1}$ during March equinox and minimizing at $60\,m\,s^{-1}$ during September equinox. The timing of this maximum is also different between the two sites; during the equinoxes, it occurs roughly 1 h earlier over Oukaïmeden than Arecibo. Again, as with the comparison to HWM14 presented above, the summer winds are different in this regard; winds measured over Arecibo have a maximum eastward wind 2 h before the maximum over Oukaïmeden. After local midnight, the magnitude and timings of the winds are in good agreement. It should be noted that some of the disagreements described above can be attributed to the differences in solar flux condition between the Morocco observations (see Fig. 3) and those presented in Fig. 8 of Brum et al. (2012). Specifically, our results were collected during the transition between a weak solar maximum and solar minimum conditions, whereas the Brum et al. (2012) results in their Fig. 8 were presented for only low and high solar flux conditions.

Yuan et al. (2013) compared the FPI measurements from Xinglong, China, at midnight local time to HWM07 by fitting three harmonics (annual, semiannual, and terannual) to the winds. We have expanded their Table 1 pertaining to the 250 km altitude to include a harmonic analysis comparison to the airglow-weighted HWM14 winds in our Table 2. We have also recalculated the amplitude and phase for HWM07 using airglow-weighting in order to best see how HWM14 has changed from HWM07. We compare this to the HWM changes seen over Oukaïmeden (from Table 1) to see how the different regions are affected. Yuan et al. (2013) found that the annual variation is dominant in the zonal winds. For the meridional winds, the amplitudes of the annual component is much smaller, although still roughly double the other two harmonic components for the meridional winds. The HWM07 prediction for the amplitude of the zonal wind annual variation was slightly too small, while its prediction was too large for the meridional wind annual variation. However, it overemphasized the semiannual variation in both directions. On the other hand, HWM14 seems to have improved in matching the semiannual variation, as the magnitudes have been significantly reduced and are much closer to the observations. However, the amplitude of the annual variation is greatly overestimated for both horizontal wind directions.

Over the Oukaïmeden Observatory, the change from HWM07 to HWM14 brought similar results. The harmonic analysis shows that the semiannual component was reduced in HWM14, compared to HWM07, in all three local times. Interestingly, the reduction in the semiannual component of zonal winds at local midnight worsens the accuracy compared to HWM07. The terannual component of the Oukaïmeden data is stronger than in the Xinglong data at local midnight, suggesting that adding a terannual harmonic to the Horizontal Wind Model could improve the fits in certain geographic regions. This result also suggests that including FPI data from the Oukaïmeden Observatory in future HWM implementations could help constrain the components of the winds and improve the African sector estimates of the 250 km neutral winds.

5 Conclusions

We have presented the first multi-year thermospheric neutral wind climatology obtained in Oukaïmeden Observatory for a period of 26 months coinciding with a solar maximum period. This climatology is useful as a validation of upper atmospheric neutral wind models over the African sector. HWM14 generally compares well with the meridional and zonal winds, but significant magnitude and phase differences remain in certain seasons. The analysis of observed climatologies from different longitude sectors that are close in either geographic or geomagnetic latitude show general sim-

ilarities but also allude to the difficulties in parsing out the control of geographically ordered versus geomagnetically ordered processes. A more comprehensive study of these effects will require additional data sources, such as those acquired from satellite platforms, and the deployment of additional ground-based instruments.

6 Data availability

The LOS wind and neutral temperature data used in this study are freely available for use in the Madrigal database http://madrigal.haystack.mit.edu/madrigal/. Please contact Jonathan J. Makela (jmakela@illinois.edu) before using these data. This work uses pyglow, a Python package that wraps several upper atmosphere climatological models. The pyglow package is open-sourced and available at https://github.com/timduly4/pyglow/. Pyglow pulls the KP, AP and $F_{10.7}$ data from NOAA's National Centers for Environmental Information: https://www.ngdc.noaa.gov/stp/geomag/kp_ap.html. The website links to a publicly available FTP page where all of the data can downloaded: ftp://ftp.ngdc.noaa.gov/STP/GEOMAGNETIC_DATA/INDICES/KP_AP.

Competing interests. The authors declare that they have no conflict of interest.

Acknowledgements. Work at the University of Illinois, including for the deployment of the instrumentation to Morocco, was supported by National Science Foundation CEDAR grants AGS 11-38998 and AGS 14-52291 as well as by NASA grant NNX14AD46G. The authors would like to thank the Oukaïmeden observatory and its staff for their support and assistance to the FPI operations. The LOS wind and neutral temperature data used in this study are freely available for use in the Madrigal database. Please contact Jonathan J. Makela (jmakela@illinois.edu) before using these data.

The topical editor, P. J. Erickson, thanks three anonymous referees for help in evaluating this paper.

References

Bilitza, D., Altadill, D., Zhang, Y., Mertens, C., Truhlik, C., Richards, P., McKinnell, L.-A., and Reinisch, B.: The International Reference Ionosphere 2012 –a model of international collaboration, Journal of Space Weather and Space Climate., 4, A07, doi:10.1051/swsc/2014004, 2014.

Brum, C. G. M., Tepley, C. A., Fentzke, J. T., Robles, E., dos Santos, P. T., and Gonzalez, S. A.: Long-term changes in the thermospheric neutral winds over Arecibo: Climatology based on over three decades of Fabry-Perot observations, J. Geophys. Res.-Space, 117, A00H14, doi:10.1029/2011JA016458, 2012.

Burke, W., Gentile, L., Huang, C., Valladares, C., and Su, S.: Longitudinal variability of equatorial plasma bubbles observed by DMSP and ROCSAT-1, J. Geophys. Res.-Space, 109, A12301, doi:10.1029/2004JA010583, 2004.

Chartier, A. T., Makela, J. J., Liu, H., Bust, G. S., and Noto, J.: Modeled and observed equatorial thermospheric winds and temperatures, J. Geophys. Res.-Space, 120, 5832–5844, doi:10.1002/2014JA020921, 2015.

Drob, D., Emmert, J., Crowley, G., Picone, J., Shepherd, G., Skinner, W., Hays, P., Niciejewski, R., Larsen, M., She, C., Meriwether, J. W., Hernandez, G., Jarvis, M. J., Sipler, D. P., Tepley, C. A., O'Brien, M. S., Bowman, J. R., Wu, Q., Murayama, Y., Kawamura, S., Reid, I. M., and Vincent, R. A.: An empirical model of the Earth's horizontal wind fields: HWM07, J. Geophys. Res.-Space, 113, A12304, doi:10.1029/2008JA013668, 2008.

Drob, D. P., Emmert, J. T., Meriwether, J. W., Makela, J. J., Doornbos, E., Conde, M., Hernandez, G., Noto, J., Zawdie, K. A., McDonald, S. E., Huba, J. D., and Klenzing, J. H.: An update to the Horizontal Wind Model (HWM): The quiet time thermosphere, Earth Space Sci., 2, 301–319, doi:10.1002/2014EA000089, 2015.

Emmert, J. T., Faivre, M. L., Hernandez, G., Jarvis, M. J., Meriwether, J. W., Niciejewski, R. J., Sipler, D. P., and Tepley, C. A.: Climatologies of nighttime upper thermospheric winds measured by ground-based Fabry-Perot interferometers during geomagnetically quiet conditions: 1. Local time, latitudinal, seasonal, and solar cycle dependence, J. Geophys. Res.-Space, 111, A12302, doi:10.1029/2006JA011948, 2006.

Fisher, D. J., Makela, J. J., Meriwether, J. W., Buriti, R. A., Benkhaldoun, Z., Kaab, M., and Lagheryeb, A.: Climatologies of nighttime thermospheric winds and temperatures from Fabry-Perot interferometer measurements: From solar minimum to solar maximum, J. Geophys. Res.-Space, 120, 6679–6693, doi:10.1002/2015JA021170, 2015.

Harding, B. J., Gehrels, T. W., and Makela, J. J.: Nonlinear regression method for estimating neutral wind and temperature from Fabry–Perot interferometer data, Appl. Optics, 53, 666–673, doi:10.1364/AO.53.000666, 2014.

Hei, M., Heelis, R., and McClure, J.: Seasonal and longitudinal variation of large-scale topside equatorial plasma depletions, J. Geophys. Res.-Space, 110, A12315, doi:10.1029/2005JA011153, 2005.

Huang, C., Burke, W., Machuzak, J., Gentile, L., and Sultan, P.: DMSP observations of equatorial plasma bubbles in the topside ionosphere near solar maximum, J. Geophys. Res.-Space, 106, 8131–8142, doi:10.1029/2000JA000319, 2001.

Link, R. and Cogger, L.: A reexamination of the OI 6300-Å nightglow, J. Geophys. Res.-Space, 93, 9883–9892, doi:10.1029/JA093iA09p09883, 1988.

Liu, H., Doornbos, E., and Nakashima, J.: Thermospheric wind observed by GOCE: Wind jets and seasonal variations, J. Geophys. Res.-Space, 121, 6901–6913, doi:10.1002/2016JA022938, 2016.

Makela, J. J. and Miller, E. S.: Influences on the Development of Equatorial Plasma Bubbles: Insights from a Long-Term Optical Dataset, in: Aeronomy of the Earth's Atmosphere and Ionosphere, 239–249, Springer, doi:10.1007/978-94-007-0326-1_17, 2011.

Makela, J. J., Ledvina, B. M., Kelley, M. C., and Kintner, P. M.: Analysis of the seasonal variations of equatorial plasma bubble

occurrence observed from Haleakala, Hawaii, Ann. Geophys., 22, 3109–3121, doi:10.5194/angeo-22-3109-2004, 2004.

Makela, J. J., Meriwether, J. W., Lima, J. P., Miller, E. S., and Armstrong, S. J.: The remote equatorial nighttime observatory of ionospheric regions project and the international heliospherical year, Earth Moon Planets, 104, 211–226, doi:10.1007/s11038-008-9289-0, 2009.

Makela, J. J., Meriwether, J. W., Huang, Y., and Sherwood, P. J.: Simulation and analysis of a multi-order imaging Fabry–Perot interferometer for the study of thermospheric winds and temperatures, Appl. Optics, 50, 4403–4416, doi:10.1364/AO.50.004403, 2011.

Makela, J. J., Meriwether, J. W., Ridley, A. J., Ciocca, M., and Castellez, M. W.: Large-scale measurements of thermospheric dynamics with a multisite Fabry-Perot interferometer network: Overview of plans and results from midlatitude measurements, Int. J Geophys., 2012, 872140, doi:10.1155/2012/872140, 2012.

Meriwether, J., Makela, J., Huang, Y., Fisher, D., Buriti, R., Medeiros, A., and Takahashi, H.: Climatology of the nighttime equatorial thermospheric winds and temperatures over Brazil near solar minimum, J. Geophys. Res.-Space, 116, A04322, doi:10.1029/2011JA016477, 2011.

Picone, J. M., Hedin, A. E., Drob, D. P., and Aikin, A. C.: NRLMSISE-00 empirical model of the atmosphere: Statistical comparisons and scientific issues, J. Geophys. Res.-Space, 107, 1468, doi:10.1029/2002JA009430, 2002.

Thompson, B. J., Gopalswamy, N., Davila, J. M., and Haubold, H. J.: Putting the "I" in IHY: The United Nations Report for the International Heliophysical Year 2007, Vol. 3, Springer Science & Business Media, 2009.

Wu, Q., Yuan, W., Xu, J., Huang, C., Zhang, X., Wang, J.-S., and Li, T.: First US-China joint ground-based Fabry-Perot interferometer observations of longitudinal variations in the thermospheric winds, J. Geophys. Res.-Space, 119, 5755–5763, 2014.

Yizengaw, E., Moldwin, M., Mebrahtu, A., Damtie, B., Zesta, E., Valladares, C., and Doherty, P.: Comparison of storm time equatorial ionospheric electrodynamics in the African and American sectors, J. Atmos. Sol.-Terr. Phys., 73, 156–163, doi:10.1016/j.jastp.2010.08.008, 2011.

Yizengaw, E., Doherty, P., and Fuller-Rowell, T.: Is space weather different over Africa, and if so, why? An AGU Chapman conference report, Space Weather, 11, 389–391, doi:10.1002/swe.20063, 2013.

Yuan, W., Liu, X., Xu, J., Zhou, Q., Jiang, G., and Ma, R.: FPI observations of nighttime mesospheric and thermospheric winds in China and their comparisons with HWM07, Ann. Geophys., 31, 1365–1378, doi:10.5194/angeo-31-1365-2013, 2013.